

Reverse-Engineering of Gradient Coil Designs Based on Experimentally Measured Magnetic Fields and Approximate Knowledge of Coil Geometry-Application in Exposure Evaluations

FENG LIU, ADNAN TRAKIC, HECTOR SANCHEZ LOPEZ, QING WEI,
MIGUEL FUENTES, EWALD WEBER, STUART CROZIER

School of Information Technology and Electric Engineering, The University of Queensland, Brisbane, QLD 4072, Australia

ABSTRACT: For many MRI installations, the coil pattern that generates pulsed magnetic fields produced by gradient coils is not provided by the manufacturer. This has implications for accurate assessments of MRI worker exposures, which is currently an important topic of research. To correctly model the level of exposure, a full three-dimensional distribution of the magnetic field in the locality of the magnet end is required, which can be difficult to obtain by experimental measurements. This research presents one possible approach, in which the prediction of a current distribution that generates an approximately identical magnetic field profile is constrained by a small number of experimentally measured magnetic field sample points within a plane outside the gradient set. The presented methodology may take into consideration other important descriptors such as field uniformity in the imaging volume, gradient coil geometry/dimension, driving current, central field strength, etc. To exemplify the application of the proposed approach, the current density and matching magnetic field distributions of x - and z -axis gradient coils are approximated without preknowledge of the gradient coil patterns for a MRI system, followed by exposure evaluations of a tissue-equivalent numerical worker model in the vicinity of said gradients. © 2009 Wiley Periodicals, Inc. Concepts Magn Reson Part B (Magn Reson Engineering) 35B: 32–43, 2009

KEY WORDS: gradient coils; worker model; measured magnetic field; reverse engineering

INTRODUCTION

As magnetic resonance imaging (MRI) technology moves into higher field strengths for improved resolution and contrast, the interaction of electromagnetic

(EM) fields generated by a new generation of imagers and occupational workers/patients has attracted significant attention (1–4).

During an MRI scan, the time-varying magnetic fields produced by the gradient coils are known to interact with the patient inside the scanner. Depending on the gradient parameters, the interaction may result in depolarization of voltage-sensitive ion channels and membranes and ensuing nerve excitation (5, 6). If uncontrolled, peripheral nerve stimulation (PNS) can range from symptoms of harmless tingling feelings in the skin, to burning sensations, and in rare cases, even pain (7, 8). According to the Institute of Electrical and Electronics Engineers (IEEE) standard (2), the in situ

Received 9 September 2008; revised 28 October 2008; accepted 30 October 2008

Correspondence to: Feng Liu; E-mail: feng@itee.uq.edu.au

Concepts in Magnetic Resonance Part B (Magnetic Resonance Engineering), Vol. 35B(1) 32–43 (2009)

Published online in Wiley InterScience (www.interscience.wiley.com). DOI 10.1002/cmr.b.20129

© 2009 Wiley Periodicals, Inc.

electric field stimulation thresholds for most central and peripheral nervous system neurons are around 12.3 and 6.15 V/m for exposure durations of 0.128 ms, respectively. However, heart and other tissues are limited to electric field exposures of 7.98 and 0.86 V/m, respectively, at a frequency of 1 kHz for controlled environments. Modern gradient coils are generally constructed according to the international standard IEC 60601-2-33 to minimize the risk of PNS.

Recently, another safety concern in MRI has been raised relating to possible gradient-pulsed magnetic field overexposure of radiographers and other occupational workers who repeatedly attend to patients during certain imaging trials (1–4). Results from the most recent studies indicate that fields produced by the gradient coils can yield similar levels of electric field/current induction in healthcare workers. This is particularly true when standing near, moving around, or bending toward the gradient set entrance, where the magnetic field gradients are naturally strongest (3). The numerical field analyses of the earlier studies (9–14) was based on theoretical gradient coil designs, as the real, practical coil patterns are, understandably, not normally provided by the manufacturer. However, a model based on an assumed gradient set may not provide the most accurate predictor of field exposure.

For a more realistic and accurate exposure evaluation of a model worker, a methodology is presented herein for reverse-engineering gradient coil sets that generate nearly identical external magnetic fields as those measured within a plane outside a gradient set installation. This approach takes into consideration a number of relevant gradient set descriptors such as field uniformity in the diameter spherical volume (DSV) region, coil geometry/dimension, gradient strength, etc, while providing an approximate, full three-dimensional (3D) distribution of the magnetic field near the coil end for a more accurate computation of worker exposures. To demonstrate the application of the outlined methodology, current density and matching magnetic field distributions of x - and z -gradient coils are predicted for a 2T MRI scanner, followed by computations of exposure of a tissue-equivalent worker model in a typical standing posture near the patient's bed/imager end.

METHODOLOGY

Prediction of Gradient Coil Pattern Based on Experimentally Measured B-Field

The methodology begins with the description of the experimental measurement of magnetic field

sample points near a commercial gradient set, which are used as design constraints in shaping of the current density distribution. Figure 1 depicts the magnetic field measurement plane near the gradient set end (here: 2 Tesla Oxford scanner at The University of Queensland, Brisbane, Australia). Each gradient coil was programmed to generate typical central field strengths of 30 mT/m. We note here that for the chosen measurement plane (i.e., x - z , $y = 0$), the magnetic field produced by the y -axis gradient coil is minuscule compared to the fields produced by other two Cartesian gradients. In fact, for transverse gradient coil design, only the x -gradient coil is of interest, as a 90 degree rotation around the axis of symmetry would engender the y -axis gradient coil. For this purpose, a patented magnetic field dosimeter (15) was employed to measure the transient magnetic field produced by the x - and z -gradient coil during the long trapezoidal train of the standard echo planar imaging (EPI) sequence. Based on the measured pulse sequence, the field amplitudes corresponding to each spatial measurement location were averaged to form the required spatial magnetic field distribution. The spatial coordinate information is deduced from the measurements made by on-board accelerometers. The dosimeter is capable of measuring exposure to static (0–7 Tesla bipolar) and time-varying magnetic fields (up to 40 kHz) while maintaining high resolution of 0.25 mT. A more detailed description of the dosimeter and the methodology of measurement are given in (16).

We begin the process of reconstituting the gradient set patterns by defining the continuous current density distribution $\vec{J}(\rho, \phi, z)$ on the primary and shielding layers of the x - and z -axis gradient coils in terms of finite Fourier series. It is assumed that $\vec{J}(\rho, \phi, z)$ is flowing in concentric cylindrical surfaces of radii ρ_n (where: $n = 1(2)$ for the primary (shielding) layer) and that the spatial distribution of \vec{J} is confined in the interval $Z_i \leq z \leq Z_f$. The variables $Z_i = -L_n$ and $Z_f = L_n$ define the initial and the final axial limits of \vec{J} for symmetric gradient coils, where $2L_n$ is the coil length of layer n . Assuming that the radial thickness of the surface is much smaller than the cylindrical radius ρ_n , then the vector current density $\vec{J}(\rho, \phi, z)$ may be described solely in terms of the azimuthal and axial components. Carlson's approach is applied to generate coils of finite length (17). The azimuthal component of the current density for instance can be expressed as a sum of orthonormal functions multiplied by the stream function coefficients a_{nq} (18):

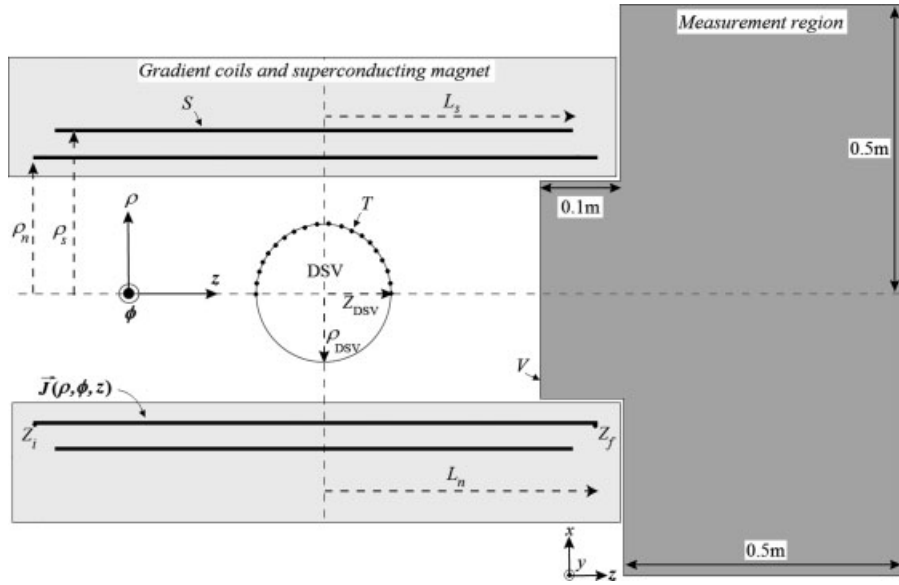


Figure 1 Diagram illustrating the cylindrical surface of radius ρ_n and length $2L_n$ where the current density \vec{J} flows. For simplicity only the surface n has been represented. The cylindrical surface of radius ρ , and axial length L_s represents the surface at the magnetic field is constrained to a minimum value (normally zero). The spherical region located at magnet iso-center represents the gradient coil DSV. The measurement region for the switched gradient coils: x - z plane ($y = 0$) is illustrated on the right.

$$J_\phi(\rho, \phi, z) = \sum_{n=1}^2 \sum_{q=1}^Q h_{nq}^\phi(\rho, \phi, z) a_{nq} \quad [1]$$

where

$$h_{nq}^\phi(\rho, \phi, z) = \delta(\rho - \rho_n) H(z) H(2L_n - z) \left\{ \begin{array}{l} \sin(k_q z) \\ \cos(k_q z) \cos(\phi) \end{array} \right\}$$

$k_q = \pi q / L_n$, a_{nq} is the amplitude of each axial oscillation mode of J_ϕ , $H(x)$ is the Heaviside function, which takes a value of 0 for $x < 0$ and 1 for $x > 0$, Q is the number of axial modes of the current density and $\delta(\rho - \rho_n) = 1$ when $\rho = \rho_n$, otherwise $\delta(\rho - \rho_n) = 0$. The upper terms in the brackets correspond to the longitudinal gradient coil and the lower to the transverse gradient coil. Because of the zero divergence of the continuity condition, the azimuthal and the axial components of $\vec{J}(\rho, \phi, z)$ are related and the coil design is completely described in terms of $J_\phi(\phi, z)$.

The magnetic field \vec{B} produced by a small superficial current element area $dS' = \rho_n d\phi' dz'$ of current density $\vec{J}(\vec{r}')$ at the observation posi-

tion \vec{r} can be computed via the Biot-Savart's method:

$$\vec{B}(\vec{r}) = \frac{\mu_0}{4\pi} \times \int_0^{2\pi} \int_{z_i}^{z_f} \frac{\vec{J}(\vec{r}') \times (\vec{r} - \vec{r}')}{\left(\rho_n^2 + \rho^2 - 2\rho_n\rho \cos(\phi - \phi') + (z - z')^2 \right)^{3/2}} ds' \quad [2]$$

Here \vec{r} and \vec{r}' denote cylindrical coordinate position vectors of the target and source field points, respectively. Expansion of the cross product in [2] will lead to the relations for the three vector components of the magnetic field, which can either be expressed in cylindrical or Cartesian coordinates depending on the requirement.

If the gradient set radii and lengths are not provided by the manufacturer, as was the case in this study, the inner bore diameter and overall length may be measured. These estimates can then be used to both enforce spatial bounds and initialize the coil dimensions within the inverse design routine. Apart from predicting the magnetic field near gradient coil

end in accordance to experimental field measurements, a set of other essential constraints were employed to assure practical solutions and these include the target gradient field strength in the DSV, minimum stray field at the inner radius of the main superconducting magnet ($\rho_s = 0.5$ m), maximum allowable coil current and adequate size of the DSV region in compliance with manufacturer's datasheets. Additional constraints may be included as required depending on the problem. The design objective can be mathematically expressed as:

$$\min \left(\omega_1 \sum_{t=1}^T |G_{x(z),t} - G_0|_{\text{DSV}}^2 + \omega_2 \sum_{s=1}^S |B_s - B^{\text{stray}}|_{\rho_s}^2 + \omega_3 \sum_{v=1}^V |B_v - B_v^{\text{meas}}|^2 \right) \quad [3]$$

where $G_x = \partial B_z / \partial x$ and $G_z = \partial B_z / \partial z$ are the spatial magnetic field B_z gradients generated by the x - and z -axis gradient coils, respectively, computed at target points T located on the half periphery of the DSV region; G_0 is the target gradient field strength in the DSV in units of T/m; B_s is the computed stray magnetic field specified at S points located at the cylindrical surface with radius ρ_s and axial length L_s ; B^{stray} is the target stray field which is here normally set to zero; B_v is the magnetic field (due to the predicted current density) at V spatial locations near gradient end within the plane illustrated in Fig. 1 (B_v is calculated using [2]); B_v^{meas} is the experimentally measured magnetic field at the same coordinates of target points V ; ω_1 , ω_2 , and ω_3 are weighting coefficients of the minimization function.

The radial and axial dimensions (ρ_n and L_n) of the primary ($n = 1$) and shielding coil ($n = 2$), and the stream function coefficients a_{nq} were then perturbed using a nonlinear least-square (LS) optimization method [19]. The objective of the design was to minimize [3], that is, to achieve a good agreement between the measured and computed magnetic field profile near the coil end within the plane illustrated in Fig. 1, while also satisfying all the other constraints in [3].

With the current density reconstituted, an approximate, full 3D distributions of the magnetic field near the gradient set end can be computed via [2] and employed in the evaluation of induced electric fields in a model worker.

Method Validation

An x -axis gradient coil (termed: target coil (A)) was designed to produce a uniform magnetic field

strength of $G_x = \partial B_z / \partial x = 30$ mT/m (with $<5\%$ peak-to-peak field variation) in a DSV region traced by $\rho_{\text{DSV}} = 0.225$ m \times $Z_{\text{DSV}} = 0.225$ m. The radii and $\frac{1}{2}$ axial lengths of the primary and shielding gradient coil layers were assumed to be $\rho_1 = 0.32$ m/ $L_1 = 0.69$ m and $\rho_2 = 0.37$ m/ $L_2 = 0.74$ m, respectively. The transport current was set to $I = 400$ Amps. The continuous current distribution was defined with a total of 12 stream function coefficients a_{nq} —i.e., six coefficients for the primary and six for the shielding coils. Then the stream function coefficients were searched using the LS routine with the objective of attaining the required spatial field uniformity/strength and maximum shielding efficacy at the inner main magnet radius as the potential eddy current source ($\rho_s = 0.5$ m, $L_s = 1$ m). For the objective function, a total of $T = 40$ and $S = 25$ sample points were used to define $\frac{1}{2}$ of the DSV periphery and shielding region, respectively. Using the solution obtained, the magnetic field B_v generated by the searched current pattern is computed near one coil end on $V = 200$ target points within a spatial region portrayed in Fig. 1. For validation purposes, this field shall be labeled B_v^{meas} (i.e., we assume that this is our “experimentally” measured field). The searched stream function coefficients of the attained solution were subsequently recorded.

To validate the proposed method, it is assumed that the x -gradient coil geometry and current pattern are unknown. We suppose, however, that B_v^{meas} in particular, the dimensions of the uniformity region and central field strength are given. For the purposes of validation, we assume that the primary and shielding coils reside in the following spatial domain: $\rho = 0.30$ – 0.42 m and $Z = 0.50$ – 0.80 m, where ρ and Z denote the radial and $\frac{1}{2}$ axial length variables, respectively. For the objective function, a total of $T = 50$, $S = 20$, and $V = 18$ sample points were used to define $\frac{1}{2}$ of the DSV periphery, shielding region ($\rho_s = 0.5$ m, $L_s = 1$ m), and the magnetic field region near the gradient coil end (see Fig. 1). In addition, for the design process, weighting factors of $\omega_1 = 1.0$, $\omega_2 = 0.9$, and $\omega_3 = 1.0$ were assigned to the DSV, shielding region, and the magnetic field near the coil end, respectively. Using the same design method, the 12 stream function coefficients, the primary and shielding coil radii and $\frac{1}{2}$ axial lengths, were perturbed with the objective to match the target B_v^{meas} with (reverse-designed) B_v (at the same coordinates of the target points V), to attain the specified spatial field uniformity/strength and minimum stray field. The outcomes of the validation (termed: reverse designed coil (B)) are provided in Results section.

Exposure of a Numerical Model Worker to Gradient-Pulsed Fields

This work considers a spatially distributed time-varying magnetic flux density that arises directly from an oscillating current in the designated x - and z -axis gradient coils. It was assumed that each gradient coil is switched trapezoidally at a frequency of 1 kHz with a gradient rise time of 250 μ s. By Faraday's law of induction, a time-varying magnetic field incident on a conductor (MRI worker) induces an in situ spatially distributed electric field/current that is also time variant. Therefore, at these low frequencies, quasi-static assumptions apply, which significantly simplifies the induction model as only resistive impedance distribution can be considered (i.e., $\epsilon = 0$).

Numerical Body Model

A heterogeneous whole-body male voxel phantom BROOK (20) was used to model the exposure of an occupational worker to gradient-pulsed magnetic fields. With forty-two tissue types identified in the model, each voxel was assigned a measured conductivity value corresponding to its dominant tissue type and appropriate to the harmonic frequency of interest (21, 22). The magnetic permeability of the body model was assumed to be same as that of air. Note here that conductivity of tissue naturally varies with frequency (see Refs. 21 and 22). Subsequently, in the realm of harmonic analysis, a time-domain pulse, such as the trapezoidal train, can be decomposed into a series (of length M) of Fourier harmonics, where it then becomes essential to scale the tissue conductivities (and other considered tissue properties) with the frequency of each Fourier harmonic that composes that series. Then, provided that the frequency of the applied pulse does not change with time, the problem can be treated linearly at each frequency. After M electromagnetic simulations for each of the harmonics, M electric field results can be simply added on component basis provided that the harmonic frequencies are in the range between 1 Hz and 1 MHz (23), which is true for the gradient coil operation in this case. With a voxel in-plane resolution of 2 mm, the dimensions of the digital model were $293 \times 170 \times 939$ voxels along the z , x , and y Cartesian axis of the MRI reference plane, respectively.

Model Exposure Setup

The gradient coils under consideration are symmetric and therefore create the same magnetic field spatial pattern and strength at both ends of the coil, while

the fields near the coil ends represent the major risk areas due to worker access. The stationary model worker is positioned to face the patient table while the body surface is 10 mm away from both the imager end and patient table (see Fig. 7). The distance between the imager end and the gradient end due to the cosmetic structure is assumed to be 100 mm, in which case the body model is in reality 110 mm away from the gradient set end. The patient table of the 2 Tesla Oxford system is 0.42 m in width and ~ 2 m in length. The central axis of the gradient set is 1.15 m above ground.

Numerical Evaluation of Exposure

At low-frequencies, the computation of the electric fields induced in the body model is best accomplished with the quasi-static finite-difference (QSFD) method. The full description of our computational methodology and verifications of the QSFD scheme can be found in Refs. 3 and 9–11. According to the International Commission for Non-Ionizing Radiation Protection (ICNIRP) guideline (23), to assess exposure thresholds, Fourier harmonic decomposition of the pulse sequence needs to be performed. For trapezoidally pulsed gradient current the Fourier series is (3, 23)

$$F(t) = \sum_{m=1}^{\infty} \underbrace{\frac{4 \sin((2m-1)\omega\tau)}{(2m-1)^2 \omega\pi\tau}}_{C_m} I \sin((2m-1)\omega t) \quad [4]$$

where I is the amplitude of the gradient coil current (in Amps), t is transient time (in s), τ is rise-time (in s), ω is the angular frequency (in rad/s), m is the order of the Fourier harmonic, and C_m is the amplitude weighting factor to the m th harmonic. Then, for each Fourier harmonic m , the vector potential \vec{A}_m due to the gradient coil can be evaluated:

$$\vec{A}_m(\vec{r}) = C_m \frac{\mu_0}{4\pi} \int \int \int \vec{I}(\vec{r}') / |\vec{r} - \vec{r}'| d^3r \quad [5]$$

where μ_0 is magnetic permeability of the air; \vec{r}' is the position vector of the gradient coil wire segment, \vec{r} is the position vector of the field point, and \vec{I} is the current flowing in the wire segment. With the computed source vector magnetic potential, the QSFD method is then employed to evaluate the scalar electric potential and thus the primary and secondary electric field in tissue (see Refs. 3 and 9–11). At least $m = 7$ Fourier harmonics were used to synthesize the

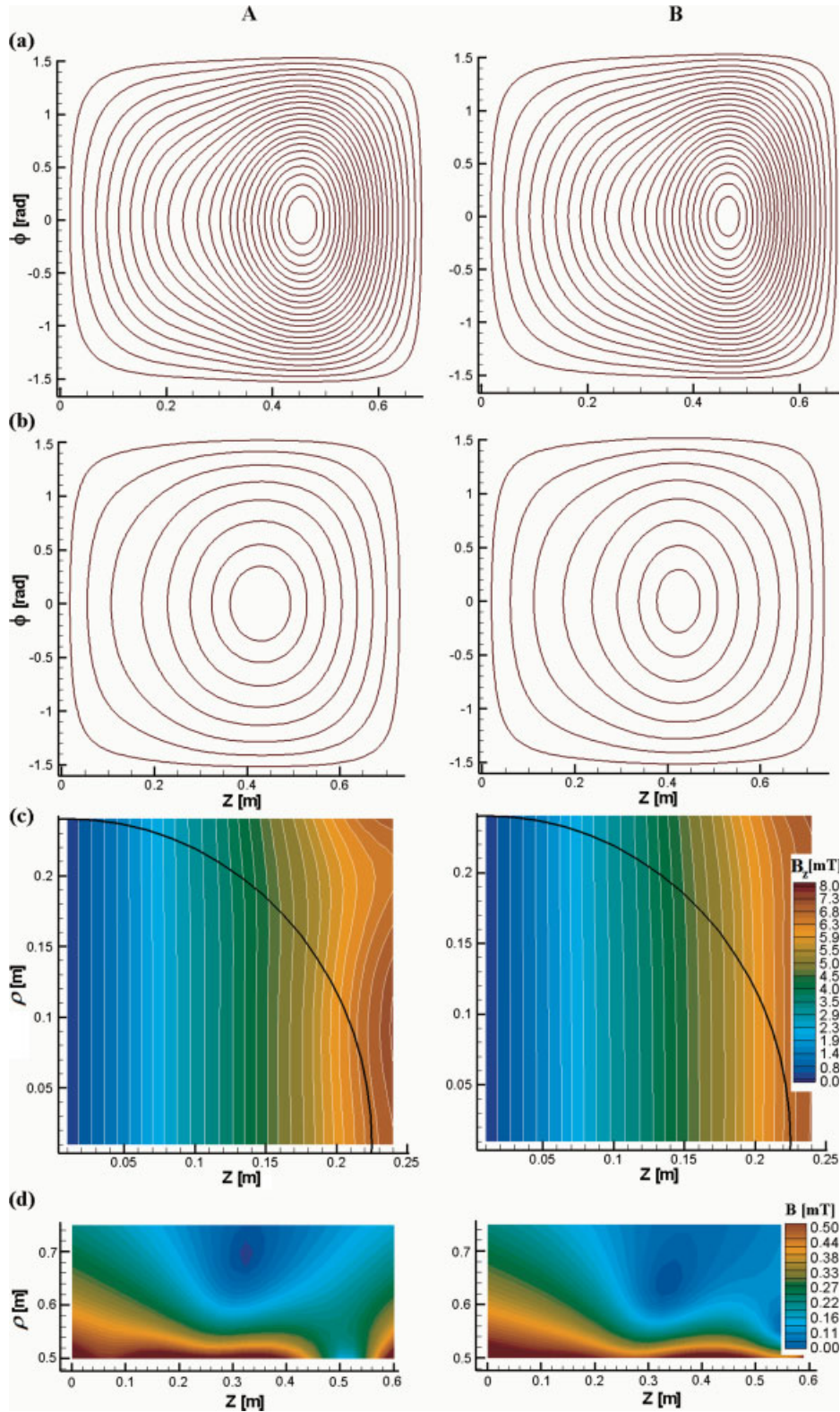


Figure 2 Comparison between the target (A) and reverse-designed (B) x -gradient coil: (a) primary coil; (b) shielding coil; (c) gradient field in the DSV region; and (d) stray field. [Color figure can be viewed in the online issue, which is available at www.interscience.wiley.com.]

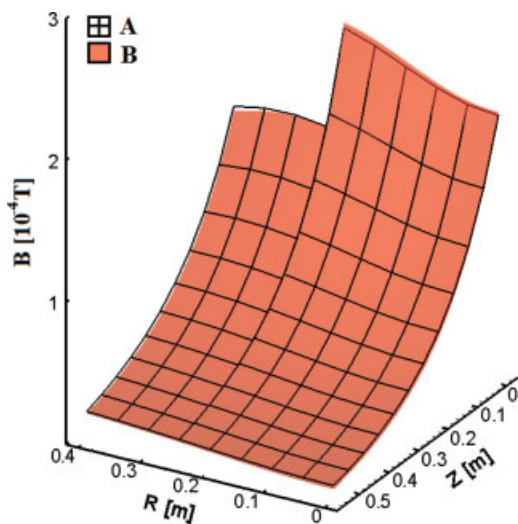


Figure 3 Comparison between the target (A) and reverse-designed (B) magnetic field near the coil end of the x -gradient coil. The results are in good agreement (the maximal difference is less than 1.2%). [Color figure can be viewed in the online issue, which is available at www.interscience.wiley.com.]

trapezoidal gradient waveform with sufficient accuracy (3).

RESULTS

Validation Results

The design results are reached in fewer than 200 iteration steps. Figure 2 shows a good agreement between the target (A) and designed (B) x -gradient coil in terms of primary and shielding coil pattern, magnetic field gradient in the imaging volume, and

the stray field in the shielding region. Both coils produce a gradient field strength of $G_x = \partial B_z / \partial x = 30$ mT/m in the predefined DSV region with less than 5%_{peak-peak} field variation. The maximum stray field at $\rho_s = 0.5$ m is around 5 Gauss. More importantly, there is a good agreement between the magnetic field spatial distributions in the vicinity of the coil end (i.e., $\|B_v - B_v^{\text{meas}}\| < 1.2\%$ _{peak-peak}), as shown in Fig. 3. It is noted that the gradient coil pattern and resulting fields are much closer to the targets if the gradient coil dimension is known. Table 1 details the geometries and stream function coefficients of both the target (A) and designed (B) x -gradient coil.

Gradient Tailoring Based on Experimentally Measured B-Field

Figure 4 shows measured spatial distribution of the magnetic field (lined plot) near the gradient set end of the 2 Tesla Oxford scanner produced by the x -axis and z -axis gradient coil. In fewer than 400 iteration steps, a good agreement was obtained for both coils between the measured and reversely designed spatial distribution of the magnetic field in the vicinity of the coil end, as shown in Fig. 4. Furthermore, Figs. 5 and 6 demonstrate that in both cases all other design targets were attained. This includes the intended gradient field uniformity and strength in the imaging volume region, minimal stray field, and practical coil pattern.

Exposure of the Model Worker to Fields Produced by Predicted Gradient Coils

Figure 7 shows the assumed position of the numerical voxel phantom facing the patient's bed, 10 mm

Table 1 Comparison Between the Target (A) and Reverse-Designed (B) x -Gradient Coil

Parameter	Unit	A		B	
Primary coil radius	m	0.32		0.32	
Primary coil 1/2 axial length	m	0.69		0.68	
Shielding coil radius	m	0.37		0.37	
Shielding coil 1/2 axial length	m	0.74		0.75	
DSV size ($R \times 1/2Z$)	m \times m	0.225 \times 0.225		0.225 \times 0.225	
Transport current	Amp	400		400	
Stream function coefficients	Primary	69,718	Shielding	69,345	Shielding
		-41,488	15,609	-45,501	13,637
		8,456	7,153	15,888	7,881
		18,191	-7,390	11,519	-6,256
		-17,157	-763	-19,076	-4,479
	1,736	-2,963	9,174	2,969	

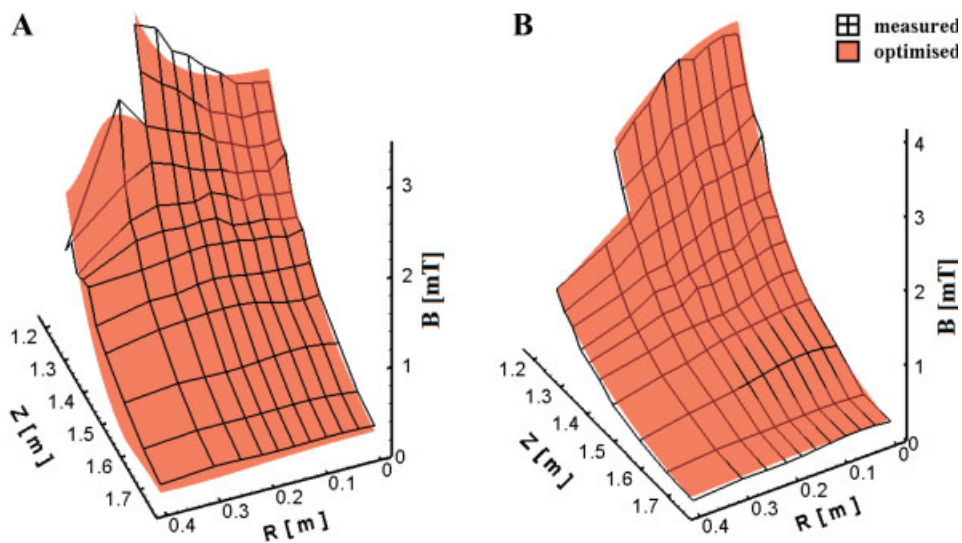


Figure 4 Comparison between the experimentally measured and predicted magnetic field of the x -axis (A) and z -axis (B) gradient coil near the coil end. The maximal difference is about 10% and it is mainly due to the measurement errors. [Color figure can be viewed in the online issue, which is available at www.interscience.wiley.com.]

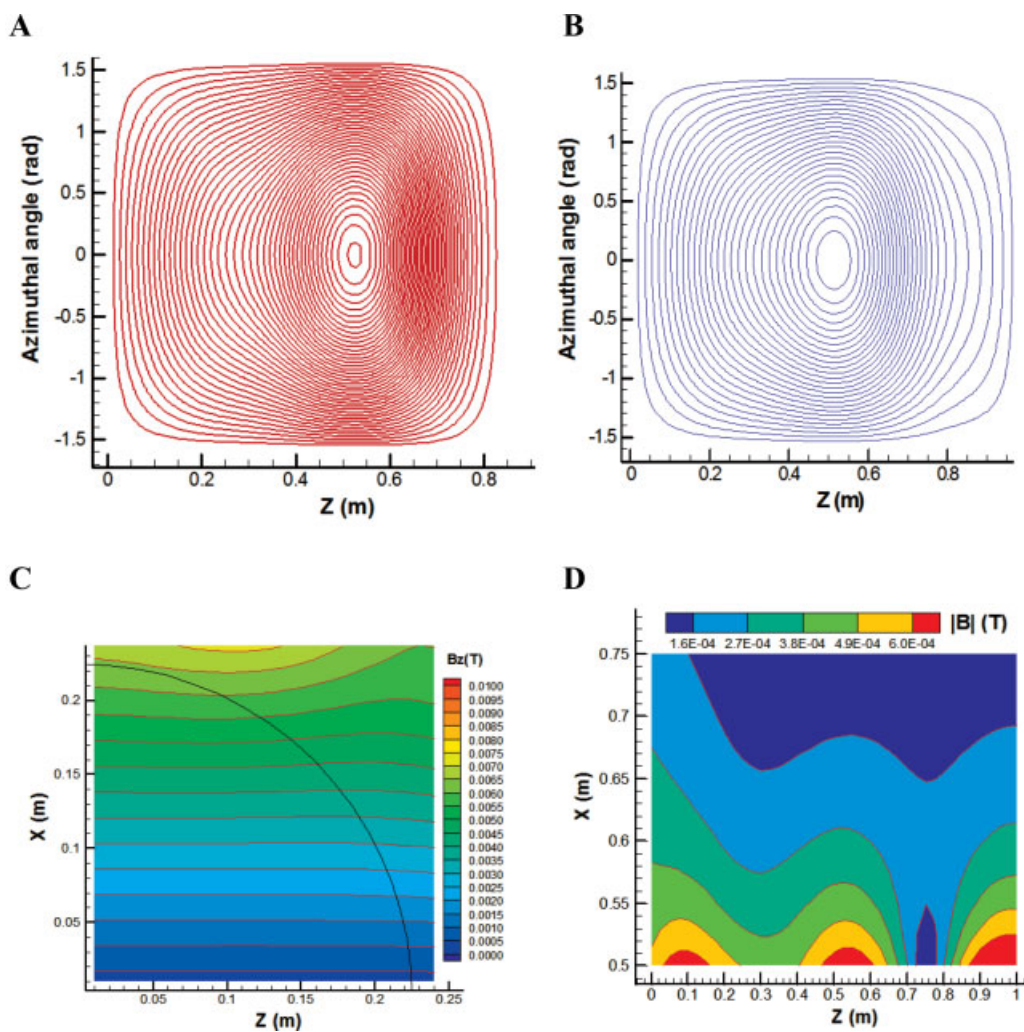


Figure 5 Predicted x -gradient coil based on experimentally measured magnetic field produced by the commercial x -gradient coil of the considered 2 Tesla Oxford system: (A) primary coil; (B) shielding coil; (C) gradient field in the DSV region; and (D) stray field. [Color figure can be viewed in the online issue, which is available at www.interscience.wiley.com.]

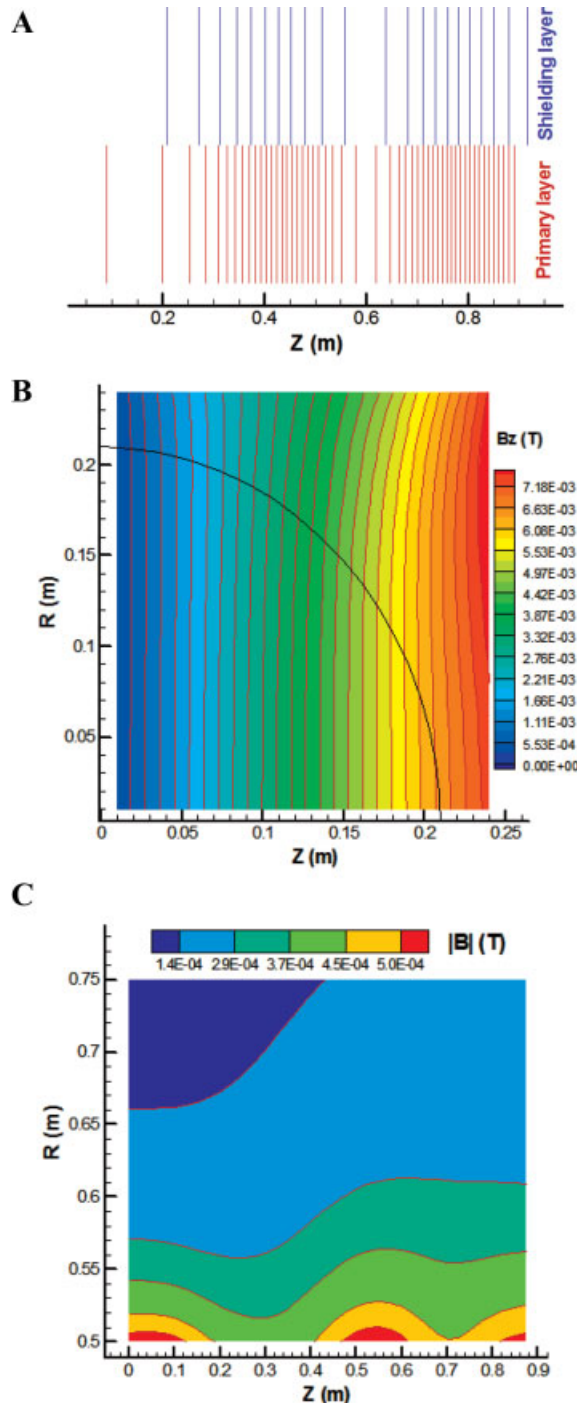


Figure 6 Predicted z -gradient coil based on experimentally measured magnetic field produced by the commercial z -gradient coil of the considered 2 Tesla Oxford system: (A) coil pattern; (B) gradient field in the DSV region; and (C) stray field. [Color figure can be viewed in the online issue, which is available at www.interscience.wiley.com.]

away from both the bed and the magnet end (including façade). This posture is intended to be typical of situations in which the medical personnel is obliged to repetitively attend anxious, sedated, or intubated patients during interventional and certain other imaging procedures. Figure 8 is an amalgamate of the induced electric field and current density distributions in central coronal, sagittal, and axial planes of the tissue-equivalent numerical worker model. We note here that the largest induced electric fields occur in body regions which are closest to the gradient coil windings (in this case, the right side of the body). Additionally, the levels of exposure are somewhat larger when the body is subject to harmonic fields produced by the longitudinal rather than the x -gradient coil.

DISCUSSION

According to the results of this preliminary study, it might be possible to mimic abstract gradient coils based on a small number of experimentally measured external magnetic field sample points without prior knowledge of the target pattern of a commercial and existing gradient coil system. To achieve a practical solution, gradient uniformity in the DSV region,

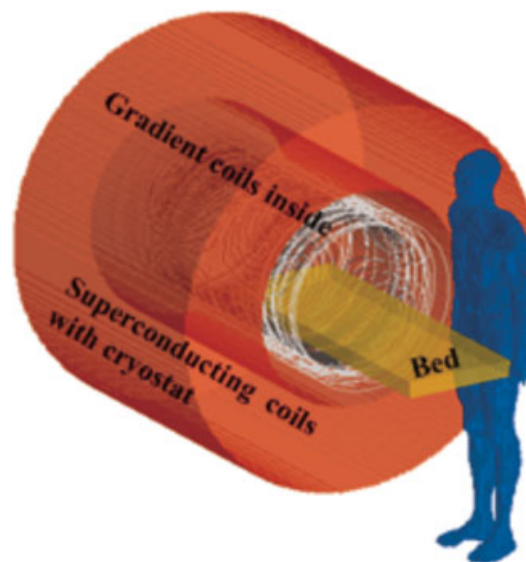


Figure 7 Assumed model worker posture near the gradient set end and patient bed. The surface of the numerical model is 10 mm away from the patient bed and imager end, respectively. The patient's bed is 0.42 m in width. [Color figure can be viewed in the online issue, which is available at www.interscience.wiley.com.]

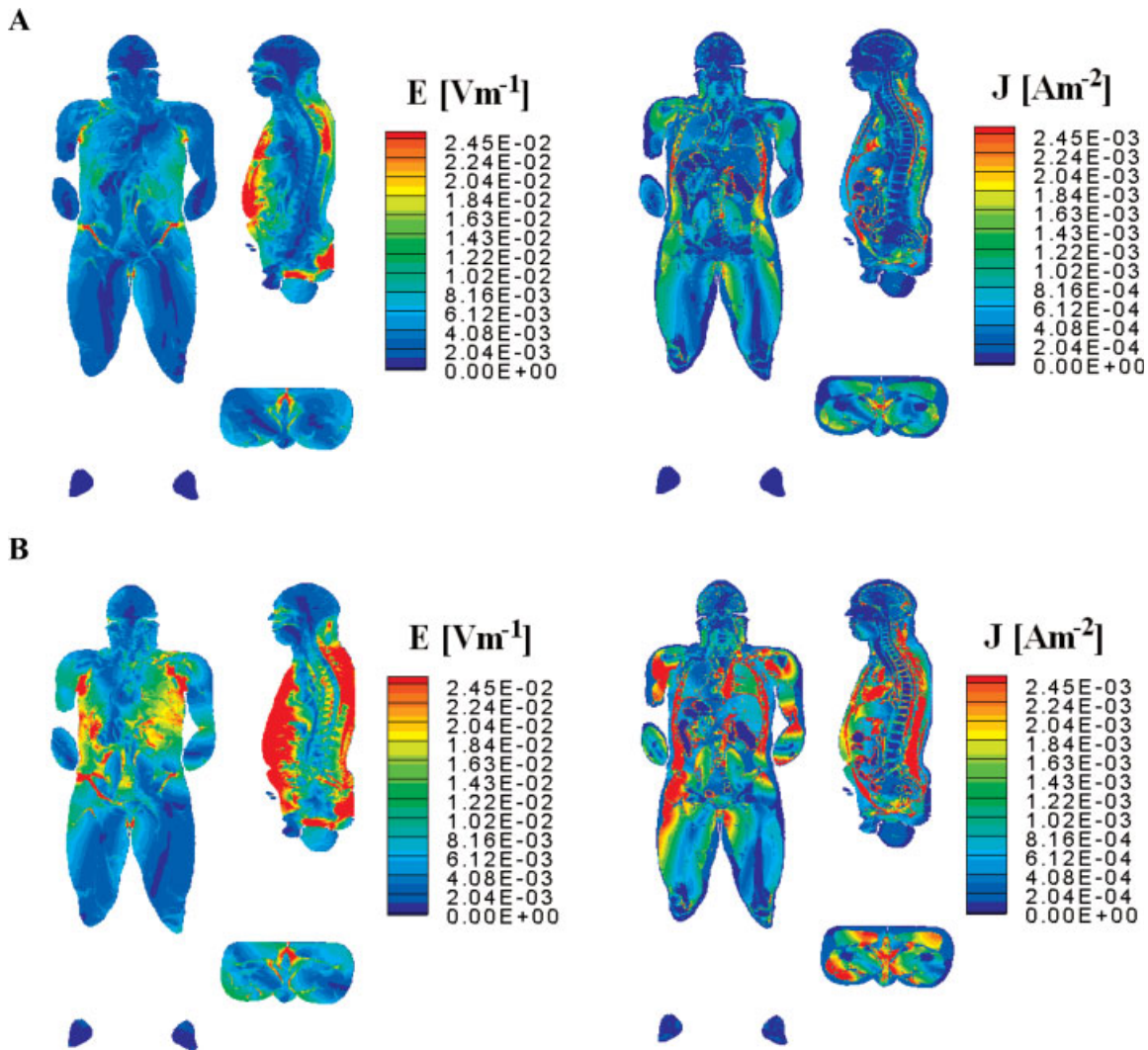


Figure 8 Coronal, sagittal, and axial electric field (left column) and current density (right column) distributions in the BROOK voxel phantom for different field exposures at 30 mT/m central gradient field strength due to (A) *x*-axis and (B) *z*-axis gradient coil. [Color figure can be viewed in the online issue, which is available at www.interscience.wiley.com.]

shielding performance, coil geometry and dimension, and transport current (as well as other constraints such as coil inductance, resistance, figure of merit, etc) may be included as part of the design objective, while predicting the spatial distribution of the magnetic field near the coil end. It should be noted, however, that increasing the number of coil descriptors would in general lead to an augmented difficulty in obtaining a satisfactory match between the target and reversely calculated magnetic field distribution at the coil end. In those instances, one might aspire to employ weighting coefficients as part of the objective function in the optimization routine. Depending on

the problem, the weighting factors can assist in achieving the right balance among the designated coil descriptors and subsequently the objective solution. More importantly, to improve the prediction of the current density and hence the approximate magnetic field distribution near the gradient coil end, one can employ a larger number of experimentally measured sample points V , possibly within a set of measurement planes or within a predefined volume. In addition, the selected target points need to be properly distributed within the designated region of interest—obviously, more samples should be allocated to regions of high spatial gradients in the external magnetic field.

With the predicted current density distribution, the three-dimensional magnetic field near the coil end can be evaluated and subsequently employed in the numerical approximation of model worker exposures to switched fields produced by realistic cylindrical gradient coils. It is noted that these preliminary field induction results are not representative of the entire body model population available and therefore further work is required in the future to extensively model the exposure of different body models to a range of commercial gradients. This was however not in the scope of this study. However, several qualitative observations can be made. From the electric field profiles in Fig. 8, it is noted that the largest values of circumferentially induced electric field normal to the direction of applied magnetic field are localized in the outermost body surfaces. This is a consequence of Faraday's law of electromagnetic induction. Since the body model used in this study is inhomogeneous in conductivity due to different tissues, current flow is modified by the boundary conditions at these tissue interfaces. Thus, high values of induced electric field are notable on the peripheries of the trunk with low electric field values in the medial regions. Consequently, the induction of electric fields in the heart compared to other tissues close to the body surface is reasonably small. On the other hand, the peripheral nerves in the skin and subcutaneous fat in the ventral and lateral regions of the torso are exposed to notable electric fields. As the current density relates to the electric field by multiplying tissue conductivity, high values of current density occur when high values of conductivity combine with enhanced electric fields. According to the simulation results at 30 mT/m gradient field strength, 1 kHz trapezoidal switching frequency with 250 μ s gradient rise time, and the assumed body model posture, the maximum field induction in the case of the x -gradient coil did not exceed the regulatory limits (1–4). However, operating the z -gradient coil at above \sim 26 mT/m could potentially result in the excitation of peripheral nerves for the herein assumed model conditions. It is noted that these preliminary findings are quite similar to those of recent studies (14, 24), which in effect to a certain extent validate the earlier models that relied on theoretical rather than realistic gradient sets.

The proposed approach may be applied to other gradient coil geometries, including those of open systems, in the evaluation of SAR (specific absorption rate) for high frequency RF coils (12) and a range of electromagnetic compatibility problems outside of MRI applications. In the future, it

would be also of great interest to predict shielded main superconducting magnets based on experimentally measured static magnetic fields. Again, this would allow more accurate predictions of exposures of MRI occupational workers when moving through strong gradients of the static magnetic field (13).

CONCLUSIONS

A method was presented that enables more practical numerical dosimetry for professional worker exposures in MRI settings without full details of the electromagnetic source—gradient coil patterns. Based on a number of experimentally measured B-field sample points near the coil end, it is possible to predict the current density patterns on the primary and shielding layer in order to approximate the measured B-field profile while taking into account other practical gradient coil constraints. Using the derived current density distributions it is then feasible to compute the three-dimensional vector magnetic potential or magnetic field inside a tissue-equivalent body model of MRI worker near the coil end and to numerically evaluate sensible levels/profiles of induced E-fields.

ACKNOWLEDGMENTS

The authors gratefully acknowledge the financial support for this project from the Australian Research Council.

REFERENCES

1. National Radiological Protection Board (NRPB). 1993. Restrictions on Human Exposure to Static and Time-Varying Electromagnetic Fields and Radiation. Documents of the NRPB, Vol. 4, No. 5. Oxon, UK: NRPB.
2. The Institute of Electrical and Electronics Engineers (IEEE). 2002. C95.6: Standard for Safety Levels with Respect to Human Exposure to Electromagnetic Fields (0–3 kHz). New York: IEEE.
3. Health and Safety Executive. 2007. Assessment of electromagnetic fields around magnetic resonance imaging (MRI) equipment, RR570 report, Health and Safety Executive, HSE Books.
4. Directive 2004/40/EC of the European Parliament and of the Council. 2004. On the minimum health and safety requirements regarding the exposure of workers to the risks arising from physical agents (electro-

- magnetic fields). Official Journal of the European Union. L 159.
5. Hebrank FX. 2007. SAFE model—a new method for predicting peripheral nerve stimulation in MRI. In: Proceedings of the 8th Annual Meeting of ISMRM, Denver, p 8.
 6. Schaefer DJ, Bourland JD, Nyenhuis JA. 2000. Review of patient safety in time-varying gradient fields. *Magn Reson Imaging* 12:20–29.
 7. Faber SC, Hoffman A, Ruedig C, Reiser M. 2003. MRI-induced stimulation of peripheral nerves: dependency of stimulation threshold on patient positioning. *Magn Reson Imaging* 21:715–724.
 8. Bourland JD, Nyenhuis JA, Schaefer DJ. 1999. Physiologic effects of intense MR imaging gradient fields. *Neuroimaging Clin N Am* 9:363–77.
 9. Liu F, Zhao HW, Crozier S. 2003. On the induced electric field gradients in the human body for magnetic stimulation by gradient coils in MRI. *IEEE Trans Biomed Eng* 50:804–815.
 10. Liu F, Crozier S, Zhao HW, Lawrence B. 2002. Finite-difference time-domain-based studies of MRI pulsed field gradient-induced eddy currents inside the human body. *Concepts Magn Reson* 15: 26–36.
 11. Liu F, Crozier S. 2004. Electromagnetic Fields inside a lossy, multilayered spherical head phantom excited by MRI coils, models and methods. *Phys Med Biol* 49:1835–1851.
 12. Liu F, Beck BL, Fitzsimmons JR, Blackband SJ, Crozier S. 2005. A theoretical comparison of two optimization methods for radiofrequency drive schemes in high frequency MRI resonators. *Phys Med Biol* 50:5281–5291.
 13. Crozier S, Trakic A, Wang H, Liu F. 2007. Numerical study of currents in workers induced by body-motion around high-ultrahigh field MRI magnets. *J Magn Reson Imaging* 26:1261–1277.
 14. Crozier S, Wang H, Trakic A, Liu F. 2007. Exposure of workers to pulsed gradients in MRI. *J Magn Reson Imaging* 26:1236–1254.
 15. Cozier S, Wilson SJ, Gregg I. The University of Queensland. A magnetic field dosimeter. PCT/AU2005/001495.
 16. Fuentes M, Trakic A, Wilson S, Crozier S. 2008. Analysis and measurements of magnetic field exposures for healthcare workers in selected MR environments. *IEEE Trans Biomed Eng* 55:1355–1364.
 17. Carlson JW, Derby KA, Haveryszko KC, Weideman M. 1992. Design and evaluation of shielded gradient coils. *Magn Reson Med* 26:191–206.
 18. Leggett J, Crozier S, Blackband S, Beck B, Bowtell B. 2003. Multilayer transverse gradient coil design. *Concepts Magn Reson B* 16:38–46.
 19. Turner R. 1993. Gradient coil design: a review of methods. *Magn Reson Imaging* 11:903–920.
 20. Gabriel C. 1996. Compilation of the dielectric properties of body tissues at RF and microwave frequencies, Report N.AL/OE-TR-1996-0037, Occupational and environmental health directorate, Radiofrequency Radiation Division, Brooks Air Force Base, Texas.
 21. Andreuccetti D, Fossi R, Petrucci C. 2002. Dielectric properties of body tissues. Florence, Italy, Applied Physics—Italian National Research Council. Available at: <http://niremf.ifac.cnr.it/tissprop/htmlclie/htmlclie.htm#atsftag>.
 22. Gabriel C, Gabriel S, Corthout E. 1996. The dielectric properties of biological tissues, Part 1: Literature survey. *Phys Med Biol* 41:2231–2249.
 23. International Commission on Non-Ionizing Radiation Protection (ICNIRP). 1998. Guidelines for limiting exposure to time varying electric, magnetic and electromagnetic fields (up to 300 GHz). *Health Phys* 74:494–522.
 24. Trakic A, Wang H, Liu F, Sanchez Lopez H, Weber E, Crozier S. 2008. Minimizing the induced fields in MRI occupational workers by lowering the imager. *Concepts Magn Reson B* 33:39–54.